ORIGINAL ARTICLE

Design of a novel 2D ultrasonic transducer for 2D high-frequency vibration–assisted micro-machining

Vinod Satpute[1] · Dehong Huo[1] · John Hedley[1] · Mohammed Elgendy[1]

Abstract

Ultrasonic vibration–assisted machining (VAM) is a process in which a tool or workpiece is vibrated using ultrasonic frequency small-amplitude vibrations to improve cutting performance, and an ultrasonic transducer usually generates these vibrations. This study investigates how two-dimensional vibrations are generated using axially polled piezoceramics. Modifying the wave propagation in geometric ways by creating a notch at the front mass, the longitudinal response excited by the axially polled piezoceramic discs can be converted into combined longitudinal and bending vibrations at the transducer front mass. Finite element analysis (FEA) software COMSOL is used to study wave propagation, and ANSYS is used to optimize the transducer's mechanical structure, while an equivalent circuit approach is used to analyze the electrical impedance spectra and confirm its resonance frequency. An experimental analysis of impedance response and amplitude of generated vibrations using the novel 2D ultrasonic transducer is conducted to validate the numerical and analytical results, which shows that resonance frequency results are in very good agreement with the theoretical model. Finally, the proposed design is validated by preliminary test results that demonstrate its performance and principles.

1 Introduction

Vibration-assisted machining (VAM) is the process in which vibrations of regular frequencies are provided to the workpiece or the tool for better machining performance. For the suitable combination of frequency, vibration motion amplitude at the tool or workpiece and cutting velocity, the tool and workpiece lose contact which each other. Machining forces can be reduced in vibration-assisted machining process, and tool life can be increased. Also, this leads to better surface finish, improved form accuracy and zero burr formation [1–3]. A crucial component of the ultrasonic vibration–assisted machining system is an ultrasonic transducer. Based on their permanence and application requirements, a number of ultrasonic transducers are available for different vibration-assisted machining types [4]. Most of the new research in this area focuses on the Langevin transducer

because of its simple construction. It consists of piezoceramic rings sandwiched between matching end and front mass. This construction is mechanically prestressed by a centre bolt, which provides enough preload to the piezo rings to avoid any fractures on the expansion of piezoceramic [5]. One-dimensional and combined vibrations like longitudinal-flexural, longitudinal-torsional, and flexural-torsional can be generated by a single device and employed on the tool for applications like ultrasonic vibration-assisted drilling, milling, and polishing [6, 7].

Several different technologies can generate 2D vibrations. Longitudinal-bending ultrasonic vibration motion can be generated using three different methods. The first uses longitudinally polarised half-piezo rings, which produce longitudinal and bending vibrations to vibrate the tool in two directions at the resonant frequency [8, 9]. The piezoceramics can also be attached to the four sides of the beam perpendicular to each side; this design couples the two bending modes to vibrate in two directions [8]. The second method is attaching two ultrasonic transducers perpendicular or tangentially to form an elliptical motion at the tool or workpiece. This structure is most likely used in

✉ Dehong Huo
  dehong.huo@newcastle.ac.uk

[1] School of Engineering, Newcastle University,
  Newcastle upon Tyne NE1 7RU, UK

high-power applications. The drawback of these structures is the high power required to increase the performance in terms of amplitude [10]. The third method is a geometrical modification of the ultrasonic horn. The longitudinal vibrations generated by the piezoceramic stacks degenerated into longitudinal-torsional or longitudinal-bending vibrations at the tip of the horn. Geometrical modifications like a diagonal slit or spiral grooves at the outer surface of the horn and that the inner core remains as it is allows the horn to vibrate in two different directions due to wave reflection or diffraction phenomena[11, 12]. The drawback of this structure is that the generated vibrations can only be used at the tool motion, and the fabrication process is complicated.

Up to now, research has focused on the 1D resonant piezoelectric transducers for tool and workpiece motion. Some research also investigated the 2D resonant vibrations at the tool. Results obtained from 1D resonant vibrations at the tool/workpiece and 2D vibrations at the tool are shown better results than conventional machining in every aspect. Where 2D resonant vibrations at the tool even showed better results than 1D vibrations at the tool/workpiece in the aspects of cutting forces, surface roughness, and chip formation[13]. However, the 2D resonant piezoelectric transducer design to use these high-frequency ultrasonic vibrations at the workpiece instead of the tool is not established. Therefore, piezoelectric ultrasonic transducer development is required to directly assist these vibrations at the workpiece to investigate each technique's efficiency. Considering the need to investigate the 2D resonant vibration motion at the workpiece, this research aims to develop the two-mode vibrational motion piezoelectric ultrasonic transducer using the longitudinally polarised piezoceramics. As a result, this method avoids exaggerated complexity of design like non-resonant 2D vibrations generation system or generating resonant vibrations in 2D by using different piezoceramic rings. For this, a geometrical modification is proposed at the horn in this research.

2 Design of longitudinal and bending ultrasonic transducer

2.1 Material selection and design calculations

The piezoelectric ultrasonic transducer comprises piezoceramics sandwiched between a back and a front mass. A prestressed bolt is used to connect these components along with the electrodes and apply appropriate preload. The acoustic energy generated in the piezoceramics travels in both directions in the ultrasonic transducer. The front mass magnifies the vibrations generated by piezoceramics, and for this to happen, the shape of the front mass plays a crucial role. A quarter wavelength horn is normally

selected to reduce the overall volume and cost. Since the stepped horn shape has a high magnification ratio compared to other horns, it was selected in this study. In order for energy to be transferred effectively towards the front mass, the back mass' acoustic impedance must be greater than that of the front mass' [14]. Therefore, the back mass material must be denser than the front mass. Furthermore, the selected materials should satisfy the following for optimum transmission of the generated acoustic energy.

$$Z_c = \sqrt{Z_b Z_f} \tag{1}$$

where, Z_c is the acoustical impedances of piezoelectric material, Z_f is the acoustical impedance of front mass, and Z_b is the acoustical impedances of back mass. The material properties of selected materials are shown in Table 1.

As part of the research, it is proposed that the frequency of the proposed transducer be selected based on its application, vibration-assisted micro-milling. One of the most important aspects of transducer design is the dimension calculation of the back and front masses, as the resonance frequency is affected by incorrectly designed transducer parts. Ultrasonic transducers are capable of propagating various types of mechanical waves. In this transducer, longitudinal waves play the primary role since it is based on a one-dimensional model. When building ultrasonic transducers or resonators, it is important to take into account the study of wave equations for a longitudinal wave. The wavelength is determined by dividing the material's wave speed velocity by the selected resonance frequency. The overall length of the resonant transducer is indicated by this wavelength. Resonant transducers are typically built at a quarter, half, or one wavelength, so they can be attached to other devices of the same kind. Each part's length can be determined using Eqs. (3)–(6).

A variable-section bar's longitudinal vibration equation is depicted in Fig. 1 and can be determined using Newton's law.

$$\frac{\partial(S\sigma)}{\partial x}dx = S\rho\frac{\partial^2 \mu}{\partial t^2}dx \tag{2}$$

Table 1 Structure material specification of the proposed transducer [19–21]

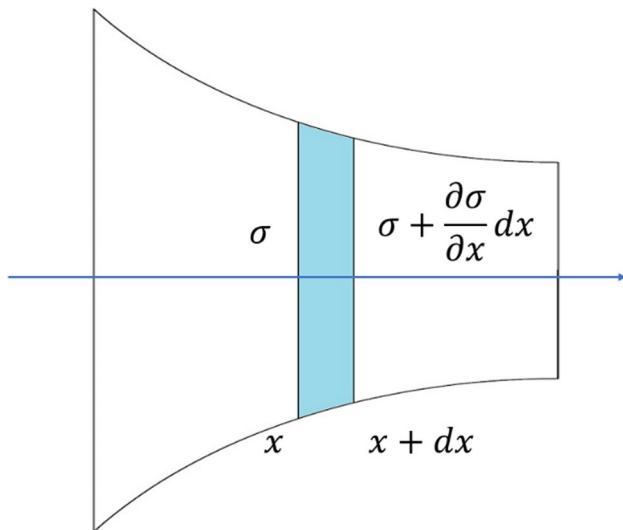| Part	Back-mass	Front-mass	Piezoceramic
Material	Ti-6Al-4V	Al7075-T6	PZT8
Young's modulus (GPa)	114	71.7	66
Density (kg/m^3)	4430	2810	7650
Sound velocity (m/s)	5072	5051	2868
Inner diameter(mm)	13	-	20
Outer diameter	52	52	50

Fig. 1 Longitudinal vibration of the bar under arbitrary cross-section

For the 1D longitudinal vibration equation of a thin section with variable cross-section, the above equation can be replaced by

$$\frac{\partial^2 \mu}{\partial t^2} + \frac{1}{S}\frac{\partial S}{\partial x}\frac{\partial \mu}{\partial x} + k^2 \mu = 0 \qquad (3)$$

where k is a wave number and expressed as $k = \omega/c$, c is sound velocity

For the uniform cross-section, $S(x) = a$, and the above equation can be replaced by

$$\frac{\partial^2 v}{\partial x^2} + k^2 v = 0 \qquad (4)$$

By applying boundary conditions to the above equation, the frequency equation calculates the length of back and front mass as stated in Eq. 5 [15–18]

$$\tan\left(\frac{\omega L_p}{c_p}\right)\tan\left(\frac{\omega L_b}{c_b}\right) = \frac{\rho_p C_p A_p}{\rho_b C_b A_b} \qquad (5)$$

where $L_p, c_p, \rho_p, A_p, L_b, c_b, \rho_b, A_b$ are the length, sound velocity, density and cross-sectional area of piezoceramic and back mass, respectively.

2.2 Acoustic wave behaviour and geometrical modification of the horn

Acoustic waves can be classified into longitudinal, transverse, and Rayleigh waves. Piezo ceramics are utilised to generate longitudinal waves in the piezoelectric ultrasonic transducer technology, which are subsequently transmitted through an ultrasonic horn for various application reasons.

A longitudinal wave moves its constituent particles in the same direction as the wave that strikes them. The material faces compressive strains as the particles grow closer to one another. When a wave travels through a material, the particles can also move apart from one another, creating tensile strains [22]. Waves can change from compression waves to tension waves when they hit boundaries, depending on the boundary conditions [23]. According to the frequency choice, horn material, and design, the longitudinal stress wave, when it strikes the front face of the horn, causes the horn to expand and contract in micro or nanometres, as shown in Fig. 2b.

One of the easiest ways to produce 2D vibrations without adding to the design's complexity is by geometric modification of the ultrasonic horn. To achieve this, a notch is cut out of the smaller cylinder of the stepped horn to generate a structural discontinuity, as seen in Fig. 2. Due to this notch, the front mass is divided into two parts. The first is the continuous part, in which the longitudinal wave can travel directly, while the other is the excess mass to that continuous part. Similar to light rays deviating from their original path when travelling through an aperture; elastic waves are diffracted through geometric discontinuities [24]. This notch causes some waves to be diffracted, with intensity decreasing in the opposite direction of the continuous component, in the so-called darkened area behind the wall of the notch. The behaviour of the wave at a continuous section, where the maximum length is approximately 10 mm from the notch to the wall of the small cylinder, is taken into consideration to anticipate the wave diffraction. The diffracted wave covers the entire front face depending on the wavelength, with the continuous region having the highest intensity. The front face expands and contracts as a result of the longitudinal wave's impact as it enters this continuous section. Direct longitudinal waves produced by piezoceramics in the surplus mass are absent because of the notch, but the longitudinal force acting on the front face varies in intensity from the top continuous part to the bottom part, as shown in Fig. 2a. Equation 6 can be used to represent this intensity. The harmonic analysis of various notch sizes is shown in Table 2.

$$I = s^2 \frac{\sin^2 \alpha}{\alpha^2} \qquad (6)$$

where, $\alpha = \frac{\pi}{d}\sin(\theta)$, d represents the length of the continuous part close to the notch, θ is the angle of the point where the intensity is being measured, and S is the length of the arc to that point from diffraction.

The wave, travelling in a stepped horn, experiences discontinuities like changing the cross-sectional area. These discontinuity cause some of the wave to reflect while the remaining wave travels through the medium. The wave's longitudinal displacement is expressed as [25]

Fig. 2 **a** Proposed ultrasonic horn structure **b** working principle of longitudinal-bending horn
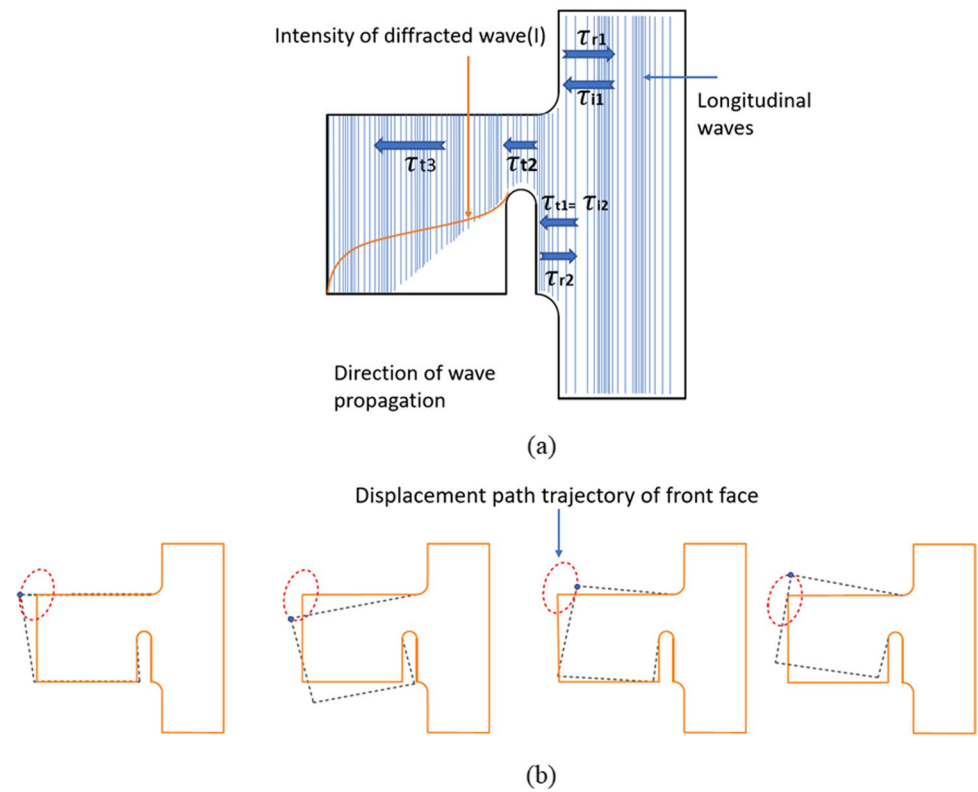

(a)

(b)

Table 2 FEA results for different notch sizes.

Sr No.	Notch size (vertical) (mm)	Notch size (horizontal) (mm)	Longitudinal displacement (um)	Bending displacement (um)
1	2	10	3.40	0.91
2	2	12	3.12	0.94
3	2	14	2.80	0.97
4	4	10	2.94	1.16
5	4	12	2.80	1.3
6	4	14	2.61	1.52
7	6	10	1.97	1.54
8	6	12	2.14	1.60
9	6	14	2.36	1.86

$$w(x, t) = A \cos (kx - kct) \qquad (7)$$

where A is amplitude and independent of x and t, A travelling wave is clearly depicted in Eq. (8) since it is the general form of $f(x\text{-}ct)$. Waves propagate with the phase velocity c when their phase $k(x—ct)$ is constant. The periodic function $w(x, t)$ represents x at any instant t with wavelength λ, where $\lambda = 2\pi/k$. A wavenumber is defined as k = 2 π/λ, which counts the number of wavelengths over 2π. When $w(x, t)$ is at any position, it has a time-harmonic relationship with time period T, where $T = 2\pi/\omega$

For mathematical convenience, Eq. (7) can be represented by

$$w(x, t) = Ae^{(ikx-ikct)} \qquad (8)$$

Then particle velocity is obtained by

$$\dot{w}(x, t) = -i\omega Ae^{(ikx-ikct)} \qquad (9)$$

Using hooks law and axial stress, which can be defined as $\varepsilon = \frac{\partial u}{\partial x}$ In Eq. (9), the corresponding stress for one-dimensional stress is then represented by:

$$\tau_i(x, t) = iEAk^{(ikx-ikct)} \qquad (10)$$

The reflected wave part is neglected. Multiplying Eq. (10) by the cross-sectional area of the rod gives the acting force:

$$F_i(x, t) = iESAk^{(ikx-ikc_0t)} \qquad (11)$$

Calculating the mechanical impedance value needed to satisfy the resonance condition involves dividing the acting force by the particle velocity. Following the notch, the transmitted wave in the cylinder can be represented by:

$$\tau_{t3} = \frac{2\rho_4 c_4 S_2}{\rho_3 c_3 S_3 + \rho_4 c_4 S_4} \tau_{i3} \qquad (12)$$

where τ represents the normal stress and i, r, and t are incident, reflected, and transmitted waves, respectively, as

shown in Fig. 2a. This thorough illustration of the longitudinal-bending horn takes into account both mechanical and electrical factors. The wave analysis that was provided was then validated using COMSOL Multiphysics' finite element approach. By using the right boundary conditions in COMSOL, elastic wave behaviour may be examined. The materials mentioned above were chosen from the material library. Physics-controlled mesh size selected, where max. and min. mesh was 5.63mm and 0.0252mm, respectively. Ten volts is applied to the piezoceramic rings, and the electrical potential is shown in Fig. 3. The generated acoustic pressure waves then travel through the front mass, aka the horn. The argument of wave behaviour above is validated through this wave propagation analysis, as shown in Fig. 4.

The travelling wave can be seen in Fig. 4d. As discussed above, the wave enters the front mass, and when the wave propagates through the notch, wave diffraction occurs. However, as shown in Fig. 4, the so-called central maxima in wave diffraction almost completely cover the front face with the highest intensity at the continuous region of the front face.

The notch's size and shape play a crucial role in the bending motion. ANSYS simulations were performed for the horn structure, and based on the ANSYS simulations, among the circular, rectangular, and triangular shapes, the circular shape near the joint is selected, which acts as the pivot point and provides a better vertical direction motion to the considered excess part at the small cylinder of the stepped horn. The front mass' ability to produce two-dimensional ultrasonic vibrations depends on the notch's horizontal and vertical dimensions. Additionally, the position of the notch relative to the front face is crucial for bending deflection. Table 2 shows different parameters used while selecting the notch size. Additionally, when designing, other elements such as the longitudinal-bending ratio, stress concentration, and potential vibration–assisted machining applications are taken into account. The recommended vibrations will not produce at the necessary frequency if the notch size is not appropriate for the design. Based on the analytical model and harmonic response in ANSYS, the notch size is chosen. The transducer's 3D model is depicted in Fig. 5.
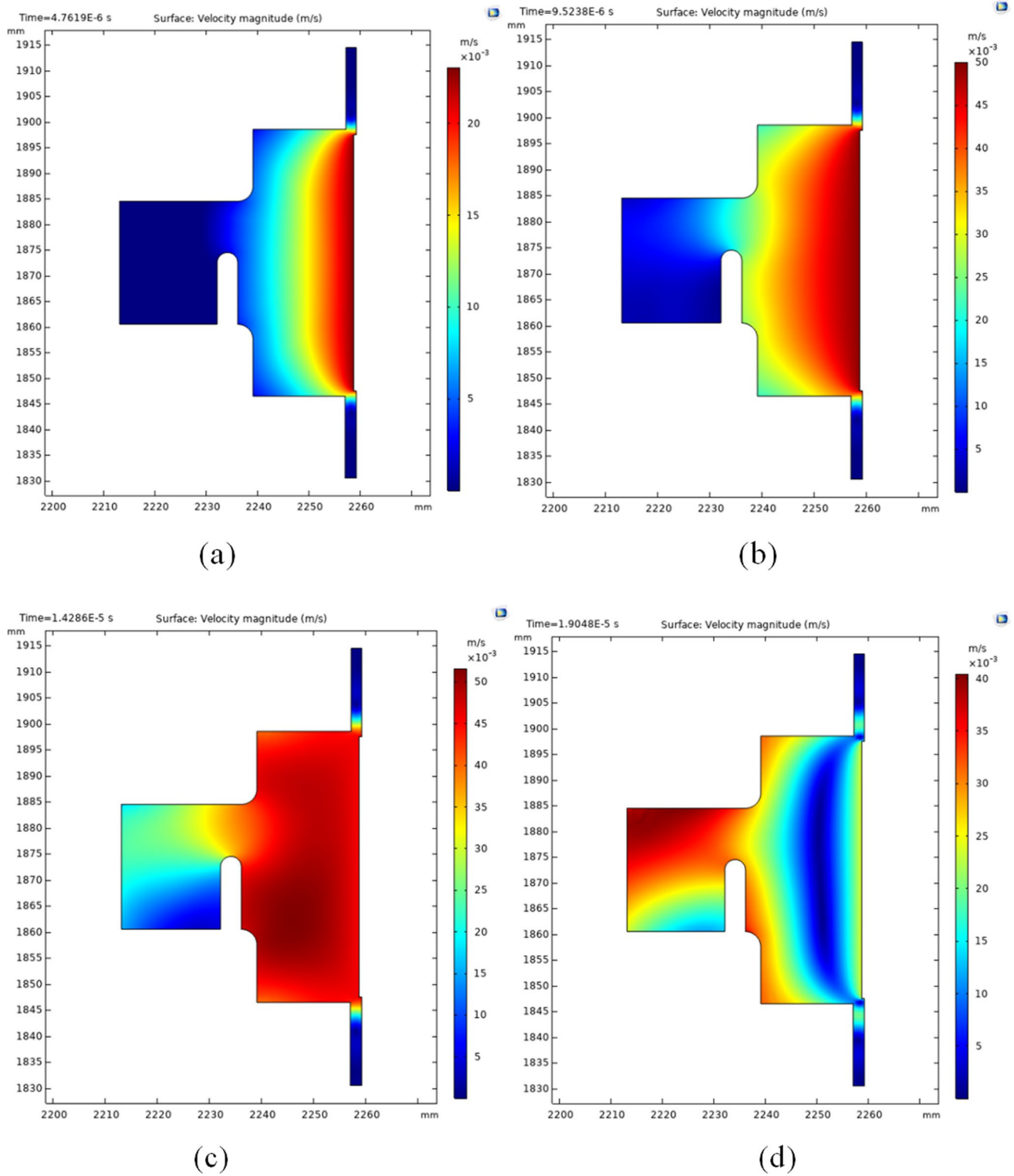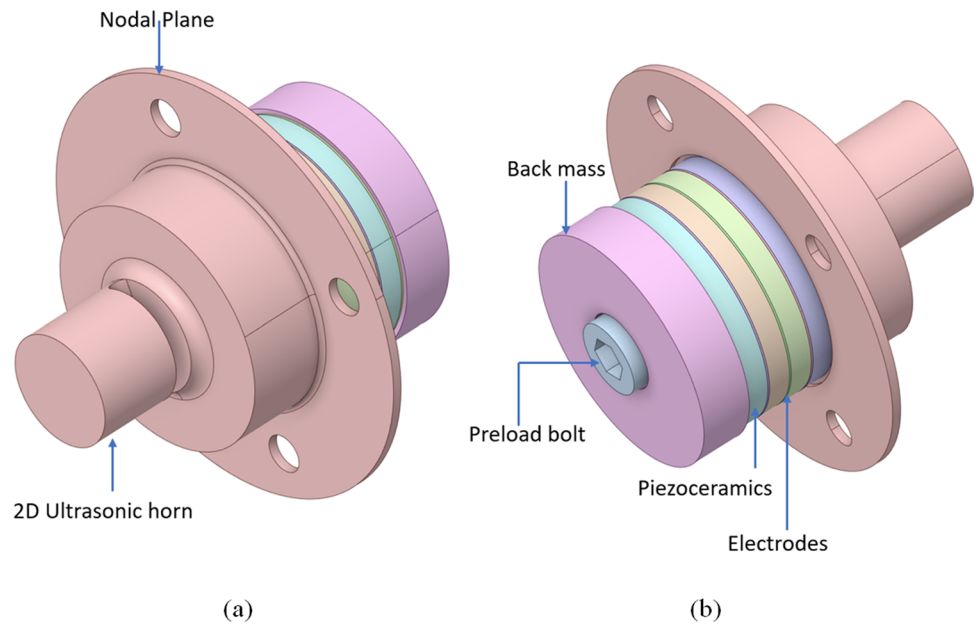

Fig. 3 Electrical potential applied to the piezoceramic
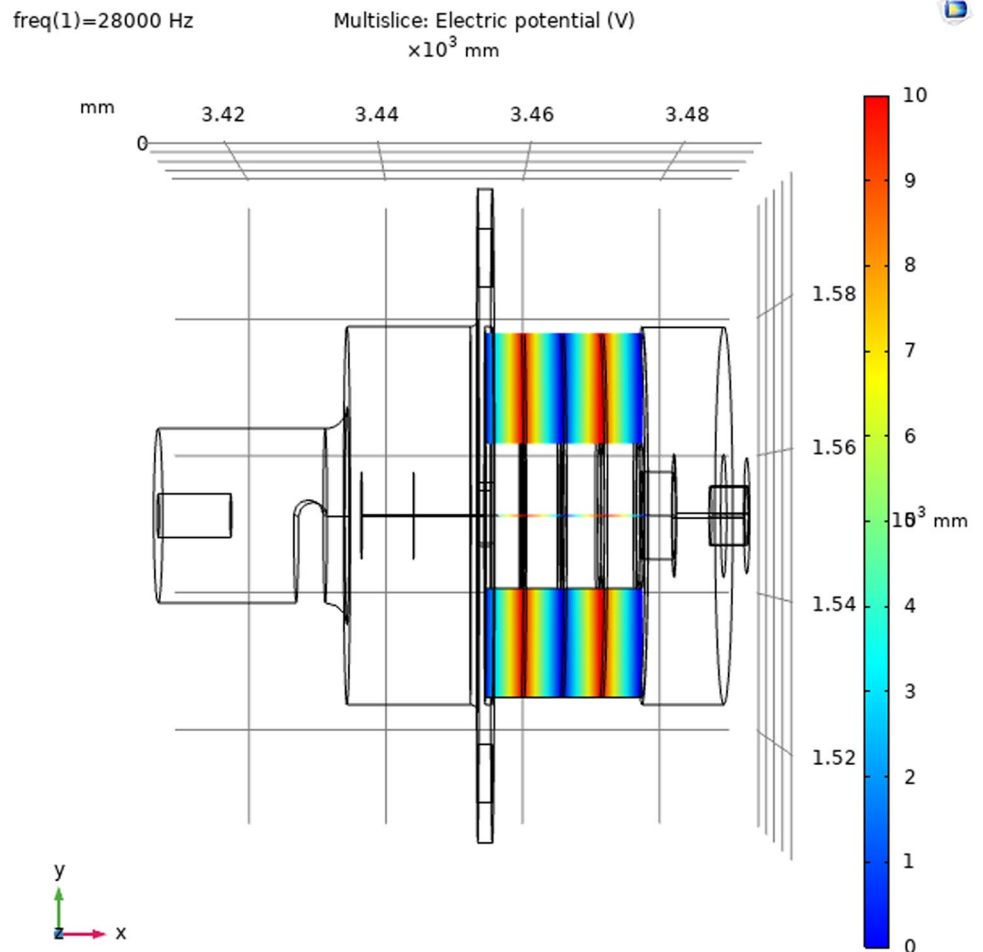
Fig. 4 Wave propagation through front mass with various time steps

Fig. 5 Proposed structure of ultrasonic transducer

(a)

(b)

To improve the front mass (horn) geometry, finite element (FE) models were created based on mechanical vibration characteristic requirements. The electrical properties of the new geometry are then predicted using the equivalent circuit approach. The combined study of analytical modelling using equivalent circuit method and numerical analysis helps verify the electromechanical parameters, like resonant frequency. Additionally, the results from these two methods can be contrasted with those from the experimental analysis in order to validate the results and identify the benefits and limitations of each technique.

Multi-component transducers require a preload because the piezoceramic rings are intrinsically weak in tension and must be kept compressed throughout the operation. The following formula can be used to determine the necessary torque T to apply to the prestressed bolt [26]:

$$T = F_t \left\{ \frac{d_2}{2} \left(\frac{\mu}{cos\alpha} + tan\beta \right) + \mu_n \frac{d_n}{2} \right\} \div 1000 \qquad (13)$$

where T is the torque [N.m], F_t is the axial tension [N], d_2 is the pitch diameter [mm], d_n is the pitch diameter of bearing surface [mm], μ is the friction coefficient of the threaded portion, μ_n is the friction coefficient of bearing portion, α is the half-angle of screw thread, and β is the lead angle.

3 Analytical approach

It is challenging to find a straightforward analytical solution to the wave equation for practical piezoelectric transducers because of the material variations, complex geometries, couplings, and discontinuities between them. Nevertheless, analytical modelling can still be done using the electromechanical equivalent circuit [17, 27]. The equivalent circuit approach uses the similarities between mechanical vibration and electrical resonance to produce an efficient mechanism for designing ultrasonic transducers. This behaviour makes it possible to represent mechanical concepts by borrowing electrical concepts. And hence it is to represent the acoustical system's impedance by using the electrical system's impedance [12].

To represent the piezoelectric transducer, there are different equivalent circuit models, namely Redwood's model, Krimholtz, Leedom, and Mattaei (KLM) model and Mason's equivalent circuit model [28–30]. The connections between mechanical, electrical, and acoustical systems can be simulated using Mason's model. Mason's model uses a six-terminal network based on the wave and piezoelectric equations and boundary conditions to represent the electromechanical behaviours of piezoelectric ceramics. The metal components of the ultrasonic transducer can be
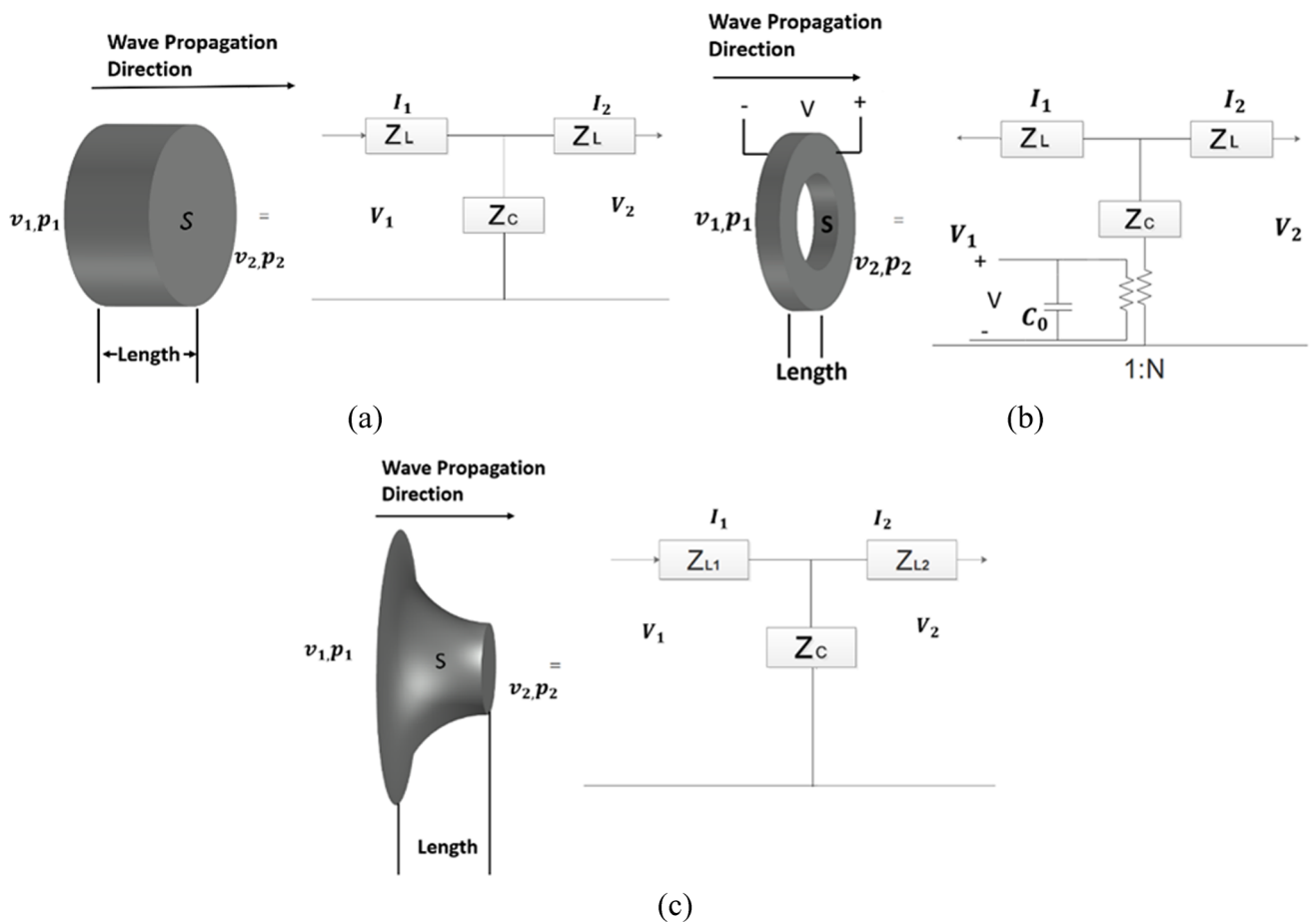
Fig. 6 Mason equivalent circuit **a** cylindrical metal part model, **b** piezoceramic model, **c** exponential structure (adapted from [14])

represented by a four-terminal equivalent circuit under the assumption of uniform stress distribution, fixed frequency, and fixed amplitude vibration of the matching mass.

An equivalent electrical T-network can give the acoustic structure as shown in Fig. 6.

As shown in Fig. 6, Z_L and Z_c represent acoustical and cross-acoustical impedances, respectively, in a uniform cross-sectional structure; the impedances are identical. $v_1 p_1$ and $v_2 p_2$ are velocity and force on the acoustical structure, which is represented by V_1, I_1 and V_2, I_2 as the equivalent voltage and current on the equivalent circuit, respectively. The terminal circuit can be represented as:

With a uniform cross-sectional structure, as depicted in Fig. 6, Z_L and Z_c stand for acoustical and cross-acoustical impedances, respectively. V_1, I_1 and V_2, I_2 are the equivalent voltage and current on the equivalent circuit, respectively, and they stand in for the velocity and force on the acoustical structure, $v_1 p_1$ and $v_2 p_2$, respectively. The terminal circuit is depicted as follows: [12, 27, 31, 32].

$$Z_L = j\rho c S \tan\left(\frac{Kl}{2}\right), \tag{14}$$

$$Z_c = \frac{-j\rho c S}{\sin(kl)} \tag{15}$$

where ρ is the density of material, c is the wave velocity, S is the cross-sectional area, k is the wavenumber, and l is the wave path length. For non-uniform cross-sections such as fillets between two different diameter parts or exponential horns, as shown in Fig. 6c, the acoustic impedance and cross-sectional impedance can be represented by:

$$Z_{L1} = j\rho c S \tan\frac{k'}{k}\left(\frac{1 - n\cos(k'l)}{n\sin(k'l)}\right) + \frac{\gamma}{K'}, \tag{16}$$

$$Z_{L2} = j\rho c S \tan\frac{k'}{kn^2}\left(\frac{n - n\cos(k'l)}{n\sin(k'l)}\right) - \frac{\gamma}{K'}, \tag{17}$$

Fig. 7 Equivalent circuit of an
ultrasonic transducer
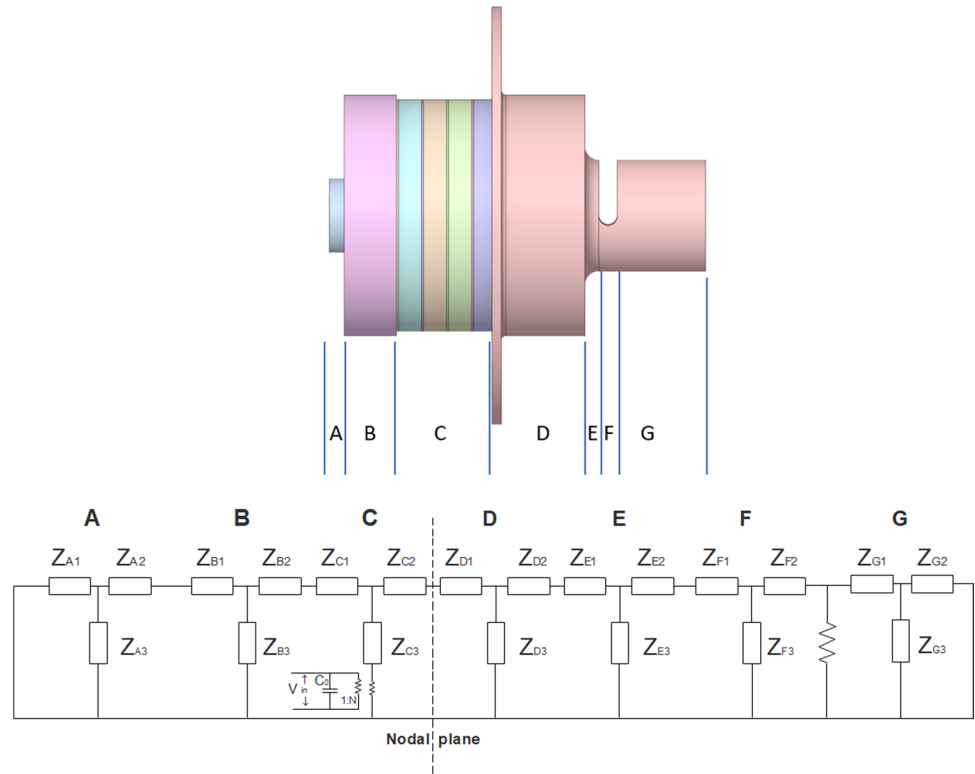
$$Z_c = -j\rho c S \frac{k'}{k n \sin(k'l)} \quad (18)$$

where γ is the area decay coefficient and k' is the root value of the difference between squares of wave number and area decay coefficient. The static capacitance value of piezoceramic stacks is expressed by:

$$C_0 = n \frac{d_{33}}{s_{33}^E} \frac{S}{t} \quad (19)$$

where d_{33} is piezoelectric charge coefficient, s_{33}^E is the elastic compliance, S is the cross-sectional area of the piezoceramic

Fig. 8 Simplified equivalent network

ring, t is the thickness of the piezoceramic ring, and n is the number of piezoceramic rings used in the transducer. Piezoelectric coupling factor N can be expressed by [33]:

$$N = \frac{nS}{L_p} \frac{d_{33}}{s_{33}^E} \quad (20)$$

By separating the transducer into seven distinct areas at the site where there is a change in material or cross-sectional area, the equivalent circuit method's concepts are applied to the device. As seen in Fig. 7, region C contains piezoceramics, electrodes, and a portion of the prestressed bolt, whereas region B contains back mass and a portion of the prestressed bolt. To calculate the mechanical impedance of this region, equivalent circuits of these regions are added in series under the premise that the strain is constant [34]. Region F represents the notch part, and region "G" represents the remaining part of the short cylinder of the stepped horn (excess mass).

The nodal plane is designed close to the back face of the front mass where piezoceramic and the front mass come into contact. At this point, there is no vibration because the amplitudes are zero. As a result, it can now be said to be an open circuit, allowing for the separation and independent analysis of each circuit on each side of the nodal plane. Furthermore, since the total loop current is zero on both sides of the nodal plane, the circuit seen in Fig. 8 can be made simpler.
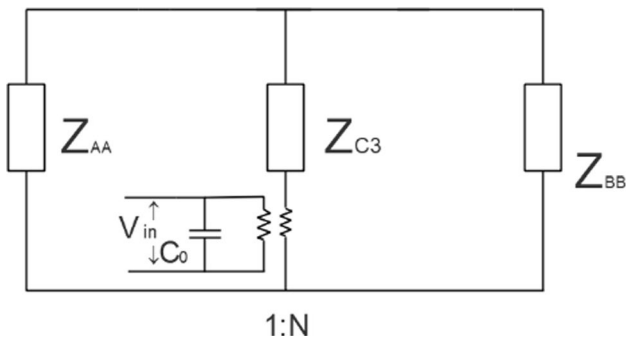
Applying Kirchhoff's current and voltage law, as shown in Fig. 8 where the value of Z_{AA} and Z_{BB} can be represented by:

$$Z_{AA} = \left[\frac{\left\{ \left(\frac{Z_{A1}.Z_{A3}}{Z_{A1}+Z_{A3}} \right) + Z_{A2} + Z_{B1} \right\}.Z_{B3}}{\left(\frac{Z_{A1}.Z_{A3}}{Z_{A1}+Z_{A3}} \right) + Z_{A2} + Z_{B1} + Z_{B3}} \right] + Z_{B2} + Z_{C1} \quad (21)$$

$$Z_{BB} = \left[\frac{\left(\left\{ \left[\frac{\left\{ \left(\frac{Z_{G2}.Z_{G3}}{Z_{G2}.Z_{G3}} \right) + Z_{G1} \right\} + Z_{F2} \right].Z_{F3}}{\left\{ \left(\frac{Z_{G2}.Z_{G3}}{Z_{G2}.Z_{G3}} \right) + Z_{G1} \right\} + Z_{F2} + Z_{F3}} + Z_{F1} + Z_{E2} \right\}.Z_{E3} + Z_{D2} \right).Z_{D3}}{\left\{ \left[\frac{\left\{ \left(\frac{Z_{G2}.Z_{G3}}{Z_{G2}.Z_{G3}} \right) + Z_{G1} \right\} + Z_{F2} \right].Z_{F3}}{\left\{ \left(\frac{Z_{G2}.Z_{G3}}{Z_{G2}.Z_{G3}} \right) + Z_{G1} \right\} + Z_{F2} + Z_{F3}} + Z_{F1} + Z_{E2} \right\}.Z_{E3} + Z_{D2} + Z_{D3}} \right] + Z_{D1} + Z_{C2} \quad (22)$$

And then, solving these circuits, the mechanical acoustic section can be calculated by:

$$Z_m = \left[\frac{Z_{AA}.Z_{C3} + Z_{BB}.Z_{C3} + Z_{AA}.Z_{BB}}{Z_{AA} + Z_{C3} + Z_{BB}} \right] \quad (23)$$

The calculated impedance is then transferred across the electrical section using the conversion coefficient:

$$Z_{mn} = \left[\frac{Z_m}{N^2} \right] \quad (24)$$

and the circuit is shown in Fig. 9.

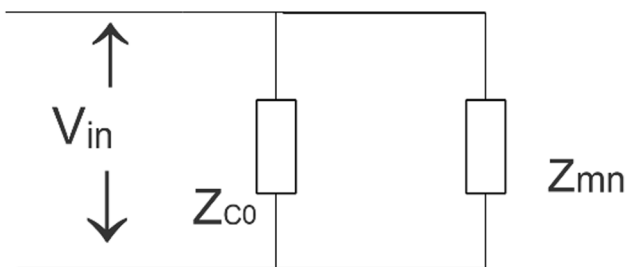Then the total impedance can be calculated by:

Fig. 9 Transferred acoustic impedance to the electric branch

$$Z_{\text{Total}} = \left[\frac{(Z_{mn}).Z_{C_0}}{Z_{mn}} \right] \quad (25)$$

The impedance at resonance and antiresonance are calculated by solving this model. The model also makes these calculations when considering the mechanical, dielectric, and piezoelectric losses as a complex form, with imaginary parts representing out-of-phase components. For

mechanical losses, the imaginary part is derived from the quality factors of the materials used, while for dielectric and piezoelectric losses, the imaginary parts are derived from the dielectric and electromechanical coupling factors. The results of calculated resonance and phase shift are as shown in Fig. 13.

4 Finite element simulation

In order to demonstrate the total effect of the notch produced for two-dimensional vibration on the transducer construction, finite element simulations using ANSYS are carried out in this work. To determine the resonance frequency and mechanical amplitude at the output front surface of the horn, modal and harmonic analyses are carried out. Additionally, node position and frequency separation were examined. Adjacent piezoceramic rings need to have polarisation directions that are the opposite in order to be excited. Since all of the transducer sections are always in bonded contact during operating settings without any separation due to the preloading condition, the contact is referred to as bonded in simulation. Mesh size is determined using the mesh convergence test and

Fig 10 **a** Model analysis of the proposed transducer. **b** Simulation model showing the working of the proposed transducer

(a)

(b)
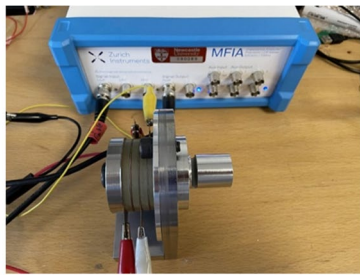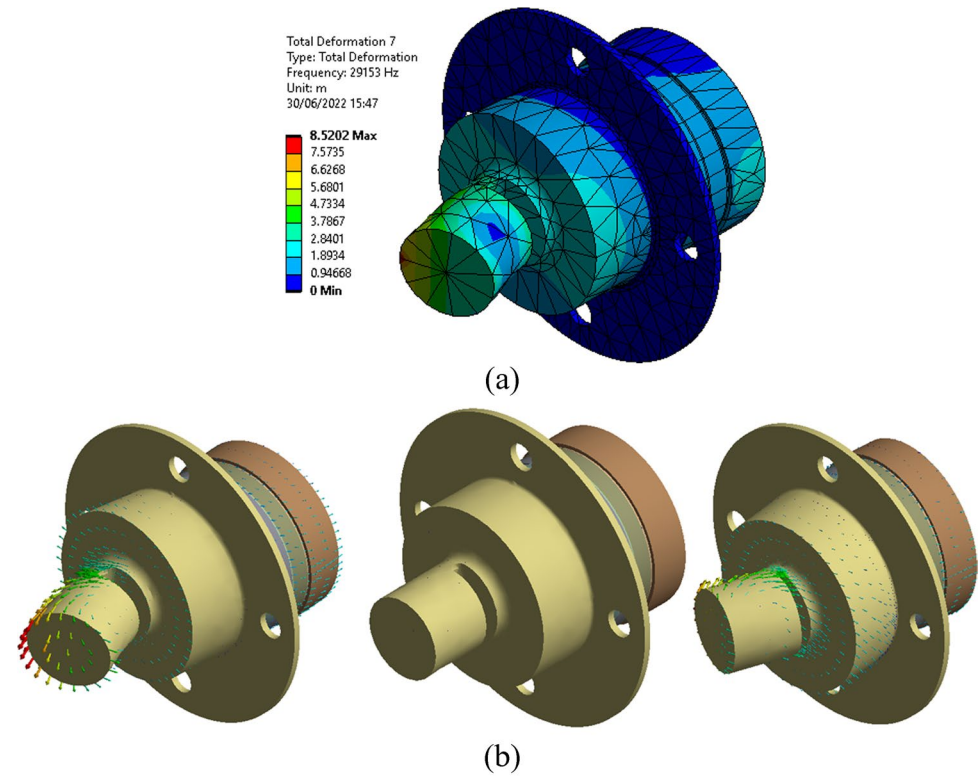
(a)
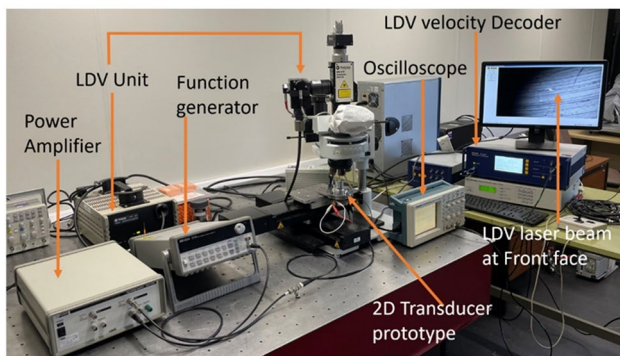
(b)

Fig. 11 Experimental setup for **a** impedance measurement and **b** vibration amplitude measurement

piezoceramics meshed by the SOLID 226 element with 20 nodes, and all other parts have meshed with solid 187 with 10 nodes. The basic tenets of finite element method theory state that the accuracy of an analysis depends on the size of the mesh elements. The theoretical model will get close to the ideal answer if the mesh element size is indefinitely small. When employed elements are too small during analysis, the meshing will produce an excessive number of elements, nodes, and degrees of freedom for the model as a whole. Due to the increased computational complexity, either it will take too long to solve the model or errors may appear. In the current modelling, the default mesh resolution size option is used with the number of elements 5623 and number of nodes 18,640. After this refinement with higher number of element and nodes which means lower size the size of element showed no improved in results.

Piezoceramic material properties like the stiffness matrix [*c*], electric matrix [*e*], and dielectric matrix [*ε*] of PZT8 are provided using ANSYS APDL commands. Figure 10 depicts the model analysis of the piezoelectric ultrasonic transducer's structure, extracted LB vibration motion, and transducer operation. The modal analysis results indicate that the notch size is appropriate for design and can produce the necessary 2D LB vibrations at the proposed frequency for its proposed application.

Fig. 12 Resonance frequency **a** equivalent circuit approach and ▶
experimental method, **b** phase shift angle, **c** current response for different voltages

Harmonic response analysis is used to study the suggested transducer, sinusoidal voltage excitation is used to determine the steady-state response of the transducer, and the resonance frequency from the modal analysis can be confirmed. Since the transducer's designed frequency is 28 kHz, a frequency range of 27 to 29 kHz with an interval of 10 Hz is chosen for the harmonic analysis. Then, using an APDL command with a 5V interval, a sinusoidal alternating voltage of between 5 and 50V is supplied to the positive electrode and a range of 0V to the negative electrode of the piezoelectric ceramic stack. The vibration amplitude is obtained at the front mass' output surface as a result of this excitation method. The outcome indicated that the chosen notch size could produce the desired displacement for the desired application.

5 Experimental analysis

Modelling of damping, dynamics of joints and other boundary conditions is challenging. Therefore, an experimental analysis should be used to verify the model. Additionally, it is employed for validation. A prototype was made based on theoretical design and numerical simulation, and the aforementioned structural parameters. Zurich Instrument-ZMFIA LCR metre 500kHz/5MHz is the impedance analyzer used to test the prototyped transducer horn in Fig. 11a. The analyzer measures the transducer's impedance to identify its resonance and antiresonance frequencies. A transducer's current is monitored while a tiny voltage (0.3 V) is supplied over a broad frequency range to ensure accurate impedance matching.

An effective design can be assessed by analysing the longitudinal and bending response to the input. In order to quantify longitudinal and bending amplitude at the front surface of the front mass, the second harmonic analysis experiment is conducted. The laser doppler vibrometer (Polytec OFV-501) is used to measure the amplitude in both directions after the transducer is excited at resonance frequency using a function generator (HP 33120A) and the signal is amplified using a TEGAM 2350 power amplifier at a voltage range of 5–50V. The longitudinal and bending vibration amplitudes were measured independently by positioning the vibrometer correctly because the vibrometer equipment utilised only measures displacement in line with the probe laser. Figure 11b shows the experimental setup for vibration amplitude measurement.

(a)

(b)

(c)
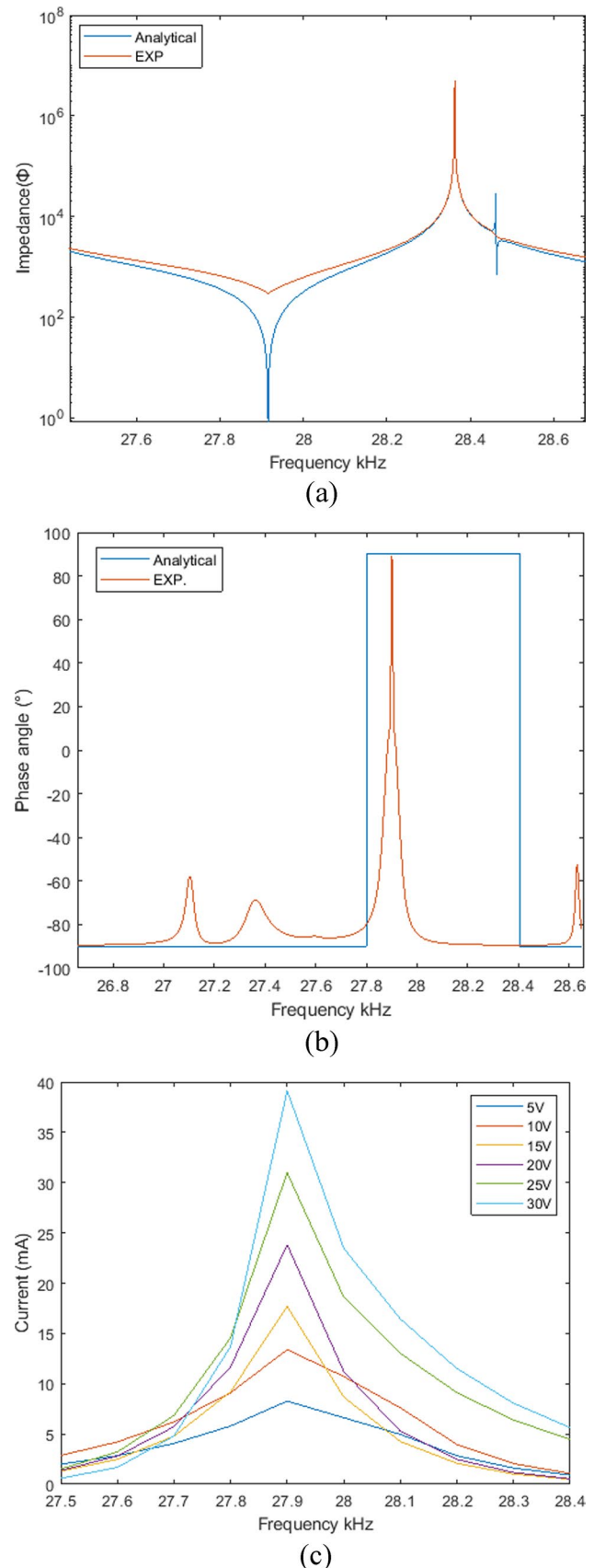
6 Transducer testing results and discussion

The resonance frequency is determined by the analytical, numerical, and experimental results and is, respectively, 27770 Hz, 28460 Hz, and 27900 Hz. This shows that there is a 0.37% difference between the design value and the resonance of the manufactured transducer. The impedance response, phase shift, and current behaviour of the resonance frequency are shown in Fig. 12a–c. The impedance value decreases to its lowest level with phase shift at the resonance frequency, satisfying the resonance criteria. Low impedance results in a rise in current at resonance, as seen in Fig. 12c. The transducer demonstrated an effective electromechanical coupling coefficient of 0.05, which indicates that it may function steadily for a considerable amount of time, according to the testing results. Real-world boundary conditions like prestress, which have an impact on the performance in real-world situations, are the cause of the minor variations between model and experimental results. Additionally, as seen in Fig. 12a–c, the experimental analysis revealed a somewhat greater impedance than the theoretical model because of the previously mentioned real-world boundary conditions. Additionally, the Q factor of the circuit is low, which has an impact on the output amplitude, according to testing results. However, despite modest variations, the resonance suggests that the better model put forward in this study has sufficient electrical characteristic prediction accuracy.

Figure 12a illustrates the impedance spectra derived from the analytical model and experiments. The analytical model and experimental results are in good agreement, which implies that for complicated transducer configurations, estimating the effective piezoelectric material properties and using a one-dimensional wave model can accurately represent the assembly's behaviour. The findings also imply that if acoustic impedance matching is taken into account when choosing materials, the assumption of perfect contact between transducer sections is accurate. The results show good agreement, indicating that it is advantageous to combine analytical and FEA models to forecast the mechanical and electrical behaviour of the transducer.

Figure 13a displays the outcomes of the experimental and FEA methodologies for the displacement of the output face of a transducer over a variety of excitation levels. Modal predictions and experimental findings agree quite well. Due to strain-electric field correlations in piezoceramics and relative motion between transducers, a few nonlinear responses are seen in the mid-and high-level excitation levels. Figure 13b and c shows longitudinal and bending motion frequency sweep displacement responses at different voltages. The results clearly show that as the transducer's impedance decreases, the front face's displacement increases, suggesting the importance of impedance matching in an electrical and mechanical system. The measured displacement response at 10V using a vibrometer and oscilloscope is shown in Fig. 13d, while Fig. 13e shows the elliptical path trajectory of the front face measured at 10V.

7 2D UVAM micro-milling tests

7.1 Experimental setup and performance analysis

An experimental setup is shown in Fig. 14. Workpiece holder is placed on the workpiece support structure and connected with the front mass using a two-headed bolt. A 20×20 mm workpiece is mounted on the workpiece holder. The workpiece holder is placed on the universal ball support structure. The whole assembly is placed on the work table of Minitech CNC minimill, which is used for the micro-milling. Using the transducer support structure, the 2D transducer is clamped on the worktable at a nodal plane. In this novel 2D ultrasonic vibration-assisted machining experiment, vibration motion at the workpiece plays a crucial part; hence, modal and harmonic analysis plays an important role in the structure design. FEA software ANSYS is used for simulation optimization of the structure. Harmonic analysis is conducted at different points on the workpiece for a uniform vibration amplitude for the slot milling experiment.

The same procedure which was used to extract the resonance frequency of the ultrasonic transducer was carried out to extract the resonance frequency of the structure. However, the whole system works on the resonance mode; hence, due to additional parts, such as the workpiece holder and workpiece, the system's resonance frequency is shifted to 30.7 kHz.

Titanium alloy is selected for the ultrasonic vibration-assisted micro-milling experiment. A solid carbide milling tool of 1.0 mm diameter is used for the micro-milling. Slot micro-milling experiments were conducted using the designed systems shown in fig.15 to examine surface roughness. For the 2D UVAMilling experiment, the new design gave the better choice of using ultrasonic vibration on the workpiece, hence two experiments; one with using vibrations in feed and cross feed direction (X–Y direction) and another with using these ultrasonic vibrations in feed and axial direction (X–Z) were conducted. 14 machining trials were conducted with combinations of machining parameters which are shown in Table 3.
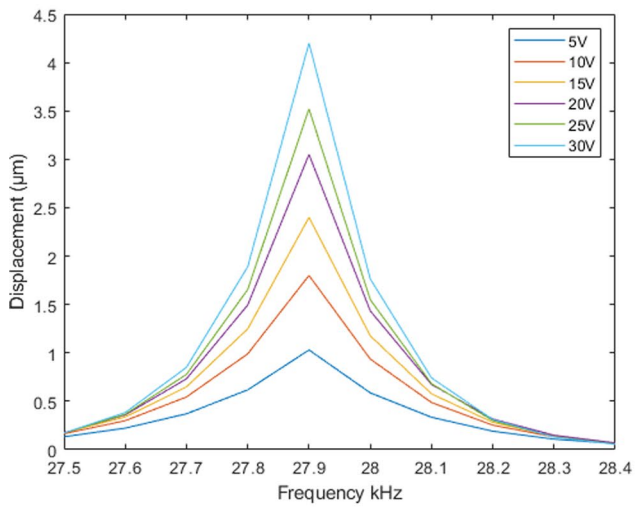
7.2 Preliminary micro-milling test results

This section aims to present experimental results from conventional machining (CM) and UVAM. As stated in Table 3, a combination of high-frequency ultrasonic vibration amplitude with different spindle speeds and feed rates is used for
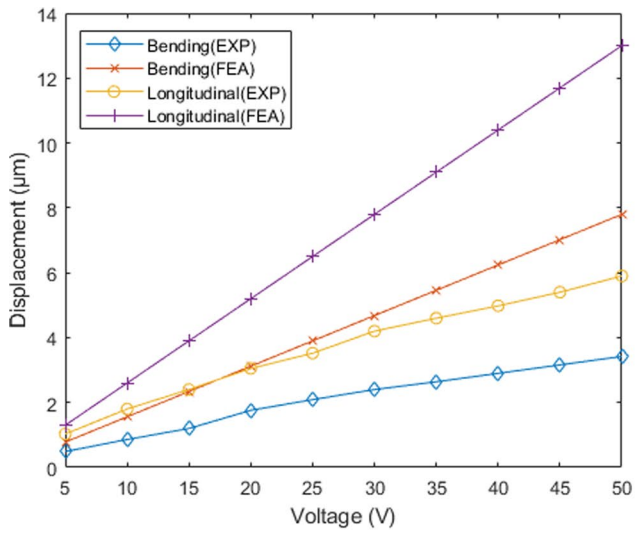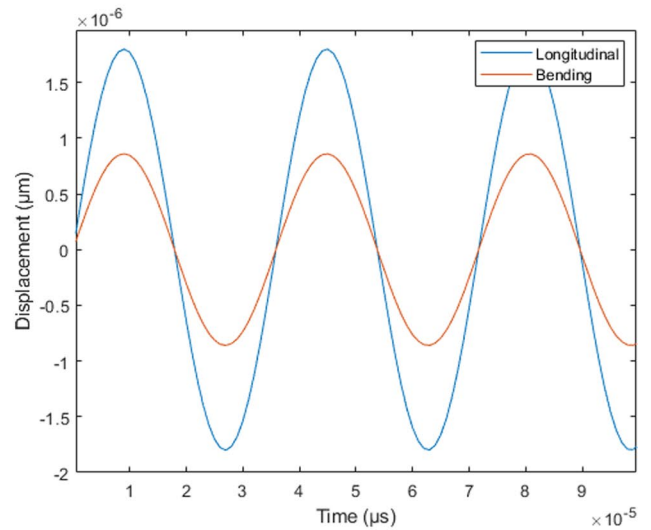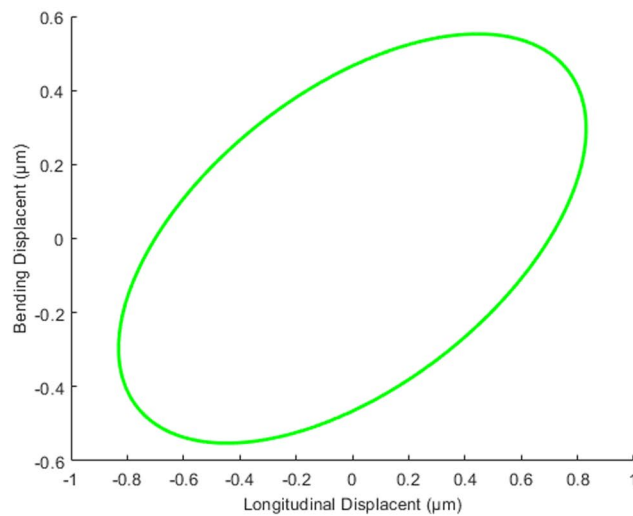
(a)
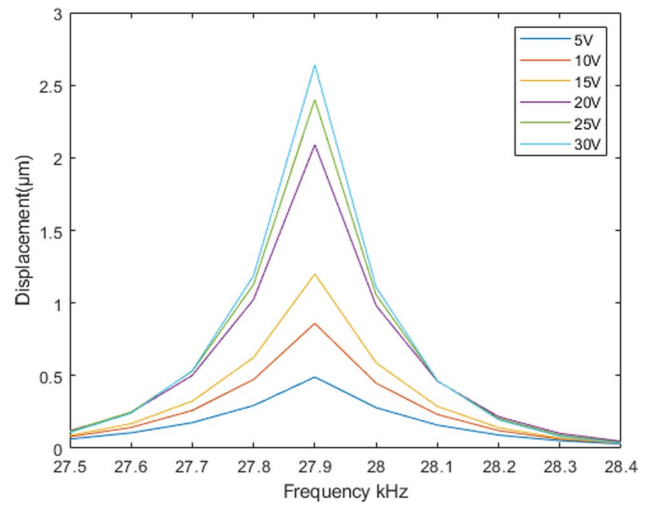
(c)

(b)

(d)

(e)

◄**Fig. 13** **a** Displacement response comparison of FEA with experimental. **b–c** Frequency sweep displacement response of longitudinal and bending motion at different voltages. **d** Measured displacement response using vibrometer at 10V. **e** Elliptical path trajectory of transducer measured at 10V
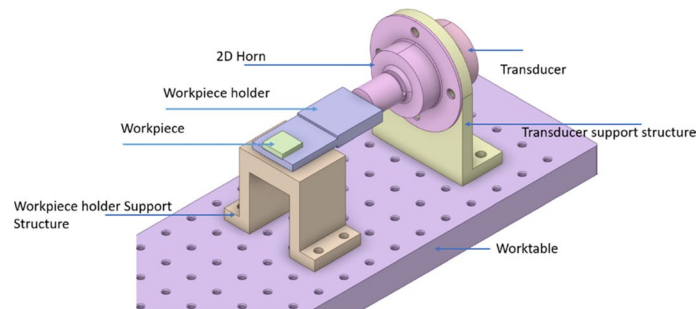
two types of 2D ultrasonic vibration-assisted machining experiments. Figure 16 shows the different elliptical paths used for machining slots. Twelve machining slots are performed on the workpiece, and a Mitutoyo surface roughness tester (SJ-410) is used to measure the surface roughness of the slot bottoms. Five surface roughness tests are performed on each slot, and their arithmetic average is taken as the surface roughness Ra value. Figure 17a shows the surface roughness results of CM and 2D UVAM when the feedrate was 5mm/min. While Fig. 17b showed similar test results when the feedrate was 10mm/min. Blue and orange colours denote the spindle speed as 15,000rpm and 30,000rpm, respectively. The longitudinal vibration amplitude corresponding to the bending one is mentioned in the bracket.

Figure 17a shows the machining experiments carried out in feed-axial (XZ) direction when the feedrate and spindle speed is 10mm/min and 30000rpm, respectively;

UVAM showed approx. 162.2% of improvement in terms of surface roughness value. When the direction of UVAM is changed to the feed–crossfeed (XY), it shows approx. 160.4% of improvement in terms of surface roughness (Ra) value. Similar results were obtained when the spindle speed decreased to 15,000rpm. Hence, the primary conclusion is drawn as, for better surface roughness (Ra) value, the direction either XY or XZ can be used for imposing ultrasonic high-frequency, low amplitude 2D vibrations on the workpiece for similar machining parameters.

Several experiments were performed by reducing the feedrate to 5mm/min in the XZ direction, and the results are shown in Fig. 17c. Comparing the results of 10mm/min feed, the surface roughness value is improved with 5mm/min and a spindle speed of 30,000rpm. With a vibration amplitude of 2 µm and spindle speed of 30,000rpm, the surface roughness value showed a further 101.2% improvement; while with a 4-µm amplitude, it showed 60% further improvement compared to the results obtained with 10mm/min feed rate and same spindle speed. Hence, the preliminary result by comparing tests nos. 1 and 2 with 13 and 14 indicates that

Fig. 14 **a** Layout of the experimental setup, **b** experimental setup. 1-Microgage dial, 2-workpiece holder, 3-2D horn, 4-transducer support structure, 5-universal ball, 6- universal ball support structure, 7- workpiece
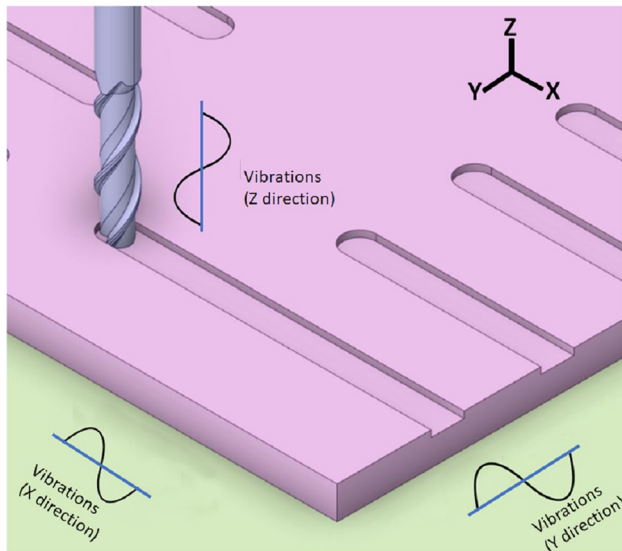

(a)
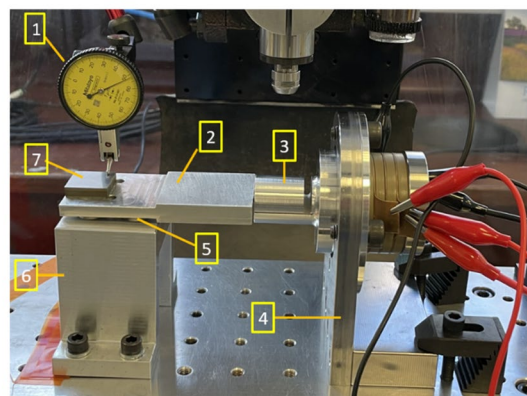
(b)

1-Microgage dial, 2-workpiece holder, 3-2D horn, 4-transducer support structure, 5-universal ball, 6- universal ball support structure, 7- workpiece

Fig. 15 Layout of milling slots showing vibration direction

better surface roughness can be achieved by imposing ultrasonic high-frequency, low amplitude 2D vibrations on the workpiece with high spindle speed and low feedrate. Figure 18 shows SEM images of slots at different location. Figure 18a, b, and c shows slots milled by CM, 2D XY UVAM, and 2D XZ UVAM respectively. It can be seen that the quality of the surface is improved using UVAM as there is a reduction in machining marks.

Furthermore, there was less edge chipping in micro milling using 2D UVAM in the XY direction, while there is a much notable difference in edge chipping in micro milling using 2D UVAM in the XZ direction.

8 Conclusion

This paper proposes an optimized novel 2D ultrasonic transducer for resonant vibration-assisted machining. A geometrically modified approach for generating 2D vibrations for elliptical motion is proposed, analyzed, and verified. The following conclusion can be drawn:

(a) A simplified design geometry, compared to other 2D resonant geometries and 2D transducers, was shown to generate an elliptical motion, which is useful for 2D resonant ultrasonic vibration-assisted machining purposes.
(b) The behaviour of acoustic wave propagation was investigated using COMSOL multiphysics, and the resonance frequencies were extracted using an equivalent circuit model, which exhibits good agreement with ANSYS and experimental testing results. This work's design methodology reveals that it is an effective method for designing 2D transducers that produce vibrations by geometrical modification.

Table 3 Vibration and machining parameters

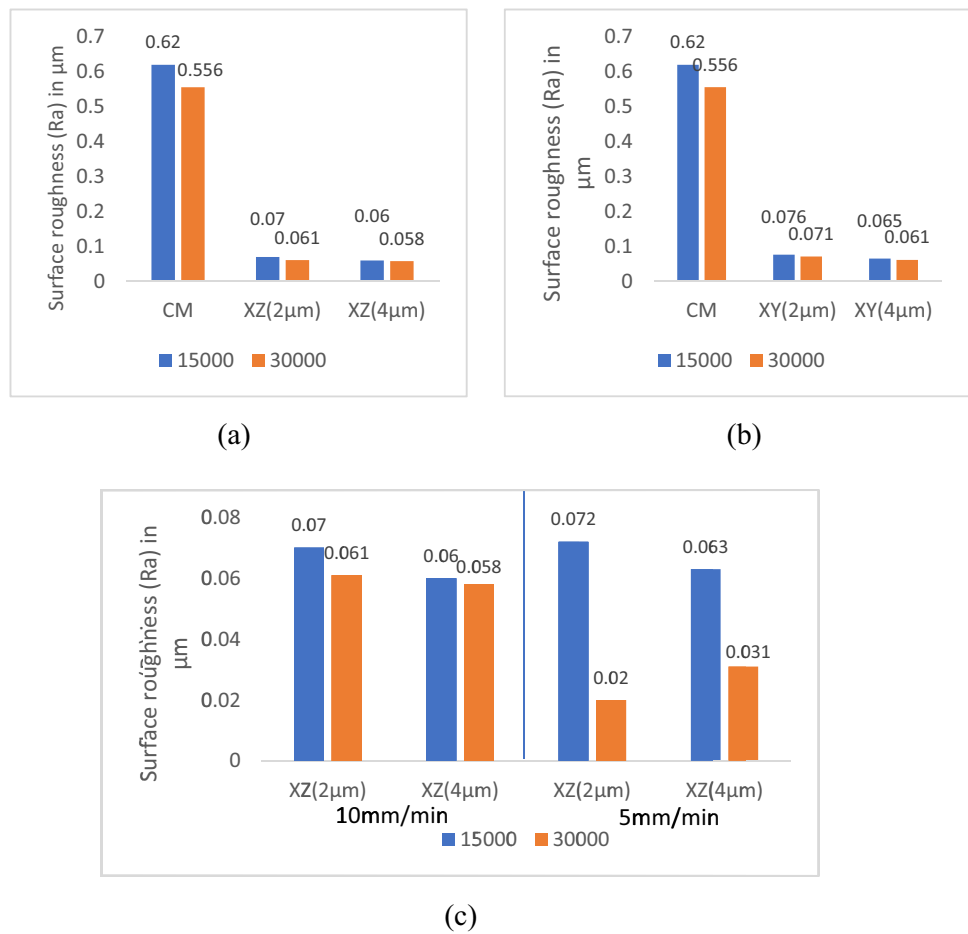| Test No.	Vibration amplitude (µm)	Vibrating direction	Vibration frequency (kHz)	Spindle speed (rpm)	Feed rate (mm/min)	Depth of cut (µm)
1	No vibration	-	-	15,000	10	30
2	No vibration	-	-	30,000	10	30
3	2	Feed-axial	30.7	15,000	10	30
4	4	Feed-axial	30.7	15,000	10	30
5	2	Feed-axial	30.7	30,000	10	30
6	4	Feed-axial	30.7	30,000	10	30
7	2	Feed-crossfeed	30.7	15,000	10	30
8	4	Feed-crossfeed	30.7	15,000	10	30
9	2	Feed-crossfeed	30.7	30,000	10	30
10	4	Feed-crossfeed	30.7	30,000	10	30
11	2	Feed-axial	30.7	15,000	5	30
12	4	Feed-axial	30.7	15,000	5	30
13	2	Feed-axial	30.7	30,000	5	30
14	4	Feed-axial	30.7	30,000	5	30
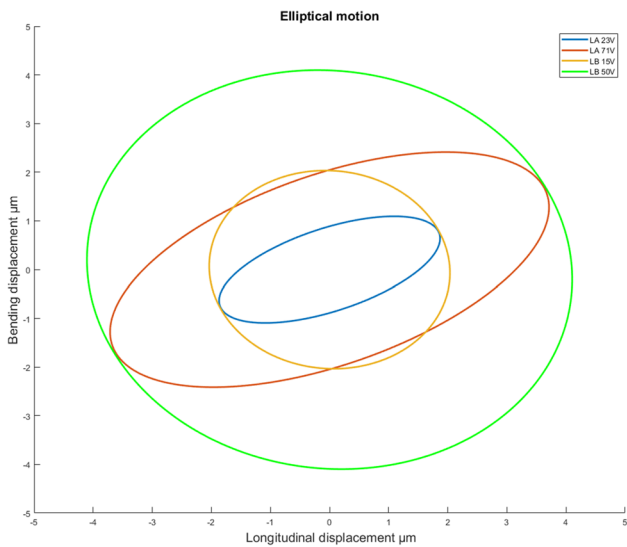
Fig. 16 Elliptical motion at a different voltage where LA—longitudinal–axial direction (Feed-axial) vibration (XZ) and LB—longitudinal–bending (feed–crossfeed) direction vibration (XY)

(c) The outcomes demonstrate that the unique method that is proposed—creating a notch on the front mass—can offer a superior option for vibration direction during vibration-assisted machining at the workpiece. Simply rotating the front mass in relation to the milling tool can provide vibration in the feed–crossfeed or feed-axial to the tool direction.

(d) A novel 2D resonant ultrasonic UVAM system is introduced in this research. Slot milling experiments with machining parameters, as mentioned in Table 3, are carried out. Based on the preliminary results mentioned in Fig. 17, the preliminary conclusion is carried out by using 2D UVAM on the workpiece, approx. 162% better surface roughness (Ra) value can be achieved by comparing the results of the same machining parameters with conventional machining (CM). From the preliminary tests, it can be concluded that for UVAM on the workpiece, either XY and XZ direction can be used as both the preliminary tests showed similar results. Also,

Fig. 17 Surface roughness (Ra). **a** Feed-axial direction, **b** feed-crossfeed direction, **c** comparison of feed-axial machining trials for different feedrates
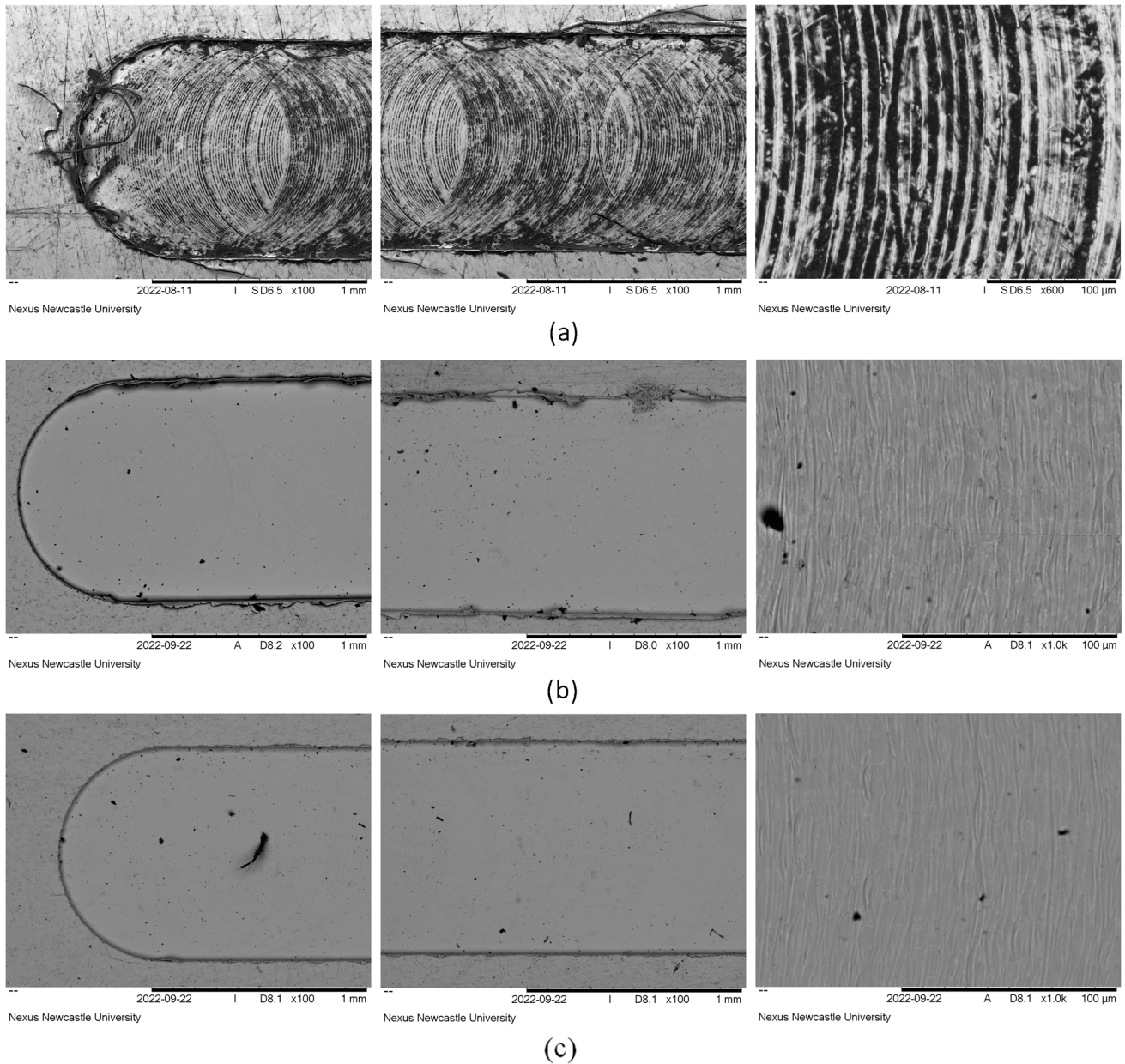
Fig. 18 Machined slots. **a** CM, **b** 2D XY UVAM, **c** 2D XZ UVAM

as mentioned in test no. 13, a low vibration amplitude of 2μm with a low feedrate of 5mm/min and high spindle speed of 30,000 in the XZ direction showed a better surface roughness (Ra) value than other parameters. Hence a preliminary conclusion was drawn for high-frequency ultrasonic vibration-assisted machining; low amplitude vibration with low feed rate and high spindle speed helps to achieve a better surface roughness (Ra) value.

(e)	Machined surface topographies are observed and compared, which showed that surface defects and machining marks could be reduced, and surface quality improved by ultrasonic vibration-assisted micro-milling.

Code availability Not applicable.

Data availability Not applicable.

Declarations

Ethics approval and consent to participate Not applicable. All authors give their permissions to participate and publish.

Competing interests The authors declare no competing interests.

References

1. Brehl DE, Dow TA (2008) Review of vibration-assisted machining. Precis Eng 32(3):153–172. https://doi.org/10.1016/j.precisioneng.2007.08.003
2. Lotfi M, Akbari J (2021) Finite element simulation of ultrasonic-assisted machining: a review. Int J Adv Manuf Technol 116:2777–279. https://doi.org/10.1007/s00170-021-07205-0
3. Kurniawan R, Ahmed F, Ali S et al (2021) Analytical, FEA, and experimental research of 2D-Vibration Assisted Cutting (2D-VAC) in titanium alloy Ti6Al4V. Int J Adv Manuf Technol 117:1739–1764. https://doi.org/10.1007/s00170-021-07831-8
4. Huo D, Zheng L, Chen W (2020) Review of vibration devices for vibration-assisted machining. Int J Adv Manuf Technol 108(5–6):1631–1651. https://doi.org/10.1007/s00170-020-05483-8
5. Arnold FJ (2008) Resonance frequencies of the multilayered piezotransducers. Proceedings - European Conference on Noise Control no. November, pp. 4209–4214. https://doi.org/10.1121/1.2934906
6. Zheng L, Chen W, Huo D (2020) Review of vibration devices for vibration-assisted machining. J Adv Manuf Technol 108(5–6):1631–1651. https://doi.org/10.1007/s00170-020-05483-8
7. Dehong Huo LZ, Chen W (2021) Vibration assisted machining (Theory, Modelling and Applications).
8. Tan R, Zhao X, Zou X, Sun T (2018) A novel ultrasonic elliptical vibration cutting device based on a sandwiched and symmetrical structure. Int J Adv Manuf Technol 97(1–4):1397–1406. https://doi.org/10.1007/s00170-018-2015-9
9. Liu J, Zhang D, Qin L, Yan L (2012) Feasibility study of the rotary ultrasonic elliptical machining of carbon fiber reinforced plastics (CFRP). Int J Mach Tool Manuf 53(1):141–150. https://doi.org/10.1016/j.ijmachtools.2011.10.007
10. Yanyan Y, Bo Z, Junli L (2009) Ultraprecision surface finishing of nano-ZrO2 ceramics using two-dimensional ultrasonic assisted grinding. Int J Adv Manuf Technol 43(5–6):462–467. https://doi.org/10.1007/s00170-008-1732-x
11. Chen T, Liu S, Liu W, Wu C (2017) Study on a longitudinal-torsional ultrasonic vibration system with diagonal slits. Adv Mech Eng 9(7):1–10. https://doi.org/10.1177/1687814017706341
12. Al-Budairi HD (2012) Design and analysis of ultrasonic horns operating in multiple vibration modes. Journal of Information Engineering and Applications. https://doi.org/10.7176/jiea/9-3-02
13. Kiswanto G, Libyawati W (2019) Fundamental aspects in designing vibration assisted machining: a review. IOP Conf Ser Mater Sci Eng 494(1):012095. https://doi.org/10.1088/1757-899X/494/1/012095
14. Shakeeb Z, Sarraf A (2019) Design and analysis of ultrasonic horns operating in multiple vibration modes. Journal of Information Engineering and Applications 2(2):28–32. https://doi.org/10.7176/jiea/9-3-02
15. Abdullah A, Shahini M, Pak A (2009) An approach to design a high power piezoelectric ultrasonic transducer. J Electroceram 22(4):369–382. https://doi.org/10.1007/s10832-007-9408-8
16. Xu J, Huanhuan R (2017) Design and finite element simulation of an ultrasonic transducer of two piezoelectric discs. Journal of Measurements in Engineering 5(4):266–272. https://doi.org/10.21595/jme.2017.19396
17. Al-Budairi H, Lucas M, Harkness P (2013) A design approach for longitudinal-torsional ultrasonic transducers. Sens Actuators A Phys 198:99–106. https://doi.org/10.1016/j.sna.2013.04.024
18. Mahdavinejad R (2005) Finite element dimentional design and modelling of an Ultrasonic Transducer, p 29
19. PZT8, Piezoceramic hard materials material data [Online]. Available: www.ceramtec.com. Accessed on 25 Dec 2019
20. Aluminum 7075-T6; 7075-T651 [Online]. Available: https://www.matweb.com/search/DataSheet.aspx?MatGUID=4f19a42be94546b686bbf43f79c51b7d. Accessed 09 Feb 2023
21. Titanium Ti-6Al-4V (Grade 5) [Online]. Available: https://www.matweb.com/search/DataSheet.aspx?MatGUID=10d463eb3d3d4ff48fc57e0ad1037434&cckck=1. Accessed 03 Jan 2020
22. Meyers MA (1994) Dynamic behavior of materials by marc andre meyers. John Wiley & Sons
23. Svensson T, Tell F (2015) Stress wave propagation between different materials, p 245
24. Mow CC, Pao YH, Achenbach JD (1971) The diffraction of elastic waves and dynamic stress concentrations. Rand Corporation Research Study 694
25. Achenbach JD (1973) Wave propagation in elastic solids. https://doi.org/10.1016/s0167-5931(13)70017-2
26. Tightening, 2-1 Various tightening methods. Tohnichi torque handbook, 9
27. Sherrit S, Leary SP, Dolgin BP, Bar-Cohen Y (1999) Comparison of the Mason and KLM equivalent circuits for piezoelectric resonators in the thickness mode. Proceedings of the IEEE Ultrasonics Symposium 2:921–926. https://doi.org/10.1109/ultsym.1999.849139
28. Redwood M (1964) Experiments with the electrical analog of a piezoelectric transducer. J Acoust Soc Am 36(10):1872–1880. https://doi.org/10.1121/1.1919285
29. Krimholtz R, Leedom DA, Matthaei GL (1970) New equivalent circuits for elementary piezoelectric transducers. Electron Lett 6(13):398–399. https://doi.org/10.1049/el:19700280
30. Mason VP (1948) Electromechanical transducers and wave filters. Van Nostrand, Princeton, N. J, pp 201–209
31. Edmonds D (1901) Experimental physics. J Am Chem Soc 23(4):281–282. https://doi.org/10.1021/ja02030a029
32. Mohammed A (1965) Equivalent circuits of solid horns undergoing longitudinal vibrations. J Acoust Soc Am 38(5):862–866. https://doi.org/10.1121/1.1909817
33. Zhang JG, Long ZL, Ma WJ, Hu GH, Li YM (2019) Electromechanical dynamics model of ultrasonic transducer in ultrasonic machining based on equivalent circuit approach. Sensors (Switzerland) 19(6). https://doi.org/10.3390/s19061405
34. Li T, Chen Y, Ma J (2009) Development of a miniaturized piezoelectric ultrasonic transducer. IEEE Trans Ultrason Ferroelectr Freq Control 56(3):649–659. https://doi.org/10.1109/TUFFC.2009.1081